



ARTICLE

# MCCGAA: Multimodal Channel Compression Graph Attention Alignment Network for ECG Zero-Shot Classification

Qiuxiao Mou, Haoyu Gui, Xianghong Tang\* and Jianguang Lu

State Key Laboratory of Public Big Data, Guizhou University, Guiyang, China

\*Corresponding Author: Xianghong Tang. Email: xhtang@gzu.edu.cn

Received: 17 November 2025; Accepted: 13 January 2026; Published: 09 April 2026

**ABSTRACT:** Electrocardiogram (ECG) is a widely used non-invasive tool for diagnosing cardiovascular diseases. ECG zero-shot classification involves pre-training a model on a large dataset to classify unknown disease categories. However, existing ECG feature extraction networks often neglect key lead signals and spatial topology dependencies during cross-modal alignment. To address these issues, we propose a multimodal channel compression graph attention alignment network (MCCGAA). MCCGAA incorporates a channel attention module (CAM) to effectively integrate key lead features and a graph attention-based alignment network to capture spatial dependencies, enhancing cross-modal alignment. Additionally, MCCGAA employs a log-sum-exp loss function, improving classification performance and convergence over the original clip-style method. Experimental results show that MCCGAA outperforms current methods, achieving the highest classification accuracy across six publicly available datasets. MCCGAA holds promise for advancing ECG zero-shot classification and offering better decision support for researchers.

**KEYWORDS:** ECG zero-shot classification; contrastive learning; cross-modal alignment; graph attention network; channel attention mechanism

## 1 Introduction

Electrocardiogram (ECG) [1] is a non-invasive graphical record of cardiac electrical signals, serving as a cornerstone for diagnosing cardiovascular diseases. ECG diagnostic classification [2] aims to categorize ECG signals into specific cardiac states or disease types. Traditional signal processing [3] and feature extraction methods rely heavily on professional domain knowledge, requiring manual design of key features such as QRS complex morphology and RR intervals. Moreover, these approaches lack robust multimodal data integration support, resulting in suboptimal efficiency and accuracy in practical applications.

Deep learning has brought transformative potential to ECG classification. Early 1D convolutional neural networks (1D-CNN) [4] excel at capturing local signal patterns, performing well in detecting ventricular and supraventricular ectopic beats. However, their inherent local receptive field limits modeling of long-term temporal dependencies and adaptation to sequence feature variations. To address this, studies combined LSTM autoencoders with SVM [5] for automatic feature learning without prior knowledge, yet these hybrid models show poor cross-distribution adaptability and fail to learn transferable features. Recently, ECG self-supervised learning (eSSL) [6,7] has gained attention for learning features from unlabeled signals. Contrastive eSSL (ceSSL) [8,9] leverages augmented sample pairs to train discriminative features, while generative eSSL (geSSL) [10] focuses on signal reconstruction for better downstream performance.

Nevertheless, eSSL methods fragment long-term ECG dependencies, losing global cardiac activity features, and lack explicit domain knowledge guidance [11], restricting zero-shot classification effectiveness.

Multimodal fusion techniques integrating ECG with clinical reports [12,13] show promise in auxiliary diagnosis [14]. Knowledge-base-enhanced approaches [15] generate expert disease descriptions to guide ECG-text joint embedding learning. However, these methods ignore spatial topological dependencies across ECG leads and patient data [16], and lack mechanisms to prioritize critical lead signals. Graph neural networks (GNNs) [17,18] excel at modeling complex multimodal relationships, yet their application in ECG-report alignment remains underexplored.

To tackle these challenges, we propose a multimodal channel compression graph attention alignment network (MCCGAA) for ECG zero-shot classification. A lightweight 1D-ResNet integrated with a channel attention module (CAM) extracts ECG features, prioritizing key leads and suppressing noise. A graph attention feature alignment network (GAFA) captures spatial topological dependencies between ECG and text embeddings for enhanced cross-modal alignment. Furthermore, we adopt a log-sum-exp contrastive loss to improve numerical stability over traditional clip-style designs. Our main contributions are summarized as follows:

1. We designed an end-to-end graph attention feature alignment network based on ECG-report dual embeddings to complement the spatial topological dependencies between modalities in the cross-modal alignment process. To our knowledge, this is the first attempt to incorporate topological dependency learning into the pre-trained ECG zero-shot classification task.
2. We designed a channel attention mechanism combined with 1D-ResNet as the ECG backbone network. Compared to the pure 1D-ResNet design, the former demonstrated superior feature extraction capabilities and provided spatial topological support for the cross-modal alignment network.
3. To enhance the stability of model training, we replaced the previously used clip-style contrastive loss function with log-sum-exp. Experimental results show that the log-sum-exp-based approach achieved better convergence and evaluation metrics.
4. We conducted evaluations on six public datasets. Experimental results show that, compared to many benchmark methods, our approach achieved promising results in most evaluation tasks, which is expected to provide better decision support for professionals in the field of ECG zero-shot classification.

The remainder of this paper is organized as follows: [Section 2](#) briefly reviews related work in ECG zero-shot classification. [Section 3](#) details the relevant design of MCCGAA, starting from the problem formulation. [Section 4](#) compares MCCGAA with the latest baseline methods on six publicly available datasets to demonstrate its effectiveness. [Section 5](#) concludes with a summary and discusses potential future research directions.

## 2 Related Works

This section reviews relevant works on ECG contrastive learning and multimodal joint learning in ECG medical diagnosis, followed by the zero-shot classification task, which is the primary focus of this study.

### 2.1 ECG Medical Diagnosis

ECG medical diagnosis analyzes ECG to assess heart health. As a convenient, inexpensive, and non-invasive tool, ECG plays a key role in early detection [19], treatment decisions, and efficacy evaluation. Multi-lead ECG provides multi-dimensional time-series signals capturing pathological features. For example, irregular R-R intervals and absent P-waves indicate atrial fibrillation; T-wave inversion or ST-segment

depression may suggest myocardial ischemia. Joint assessment of leads is complex, requires expert knowledge [19], and diagnostic accuracy is closely tied to professional expertise. Developing robust evaluation systems remains challenging.

## **2.2 Multi-Lead ECG Contrastive Learning**

ECG signal representation faces noise, complex global spatiotemporal dependencies, and high dimensionality [20]. Temporal contrastive learning (TCL) [21] optimizes representations across time segments. CLOCS [9] encourages similarity across space, time, and patients, while TS-TCC [6] uses weak and strong augmentations in cross-view prediction tasks. ASTCL [22] removes noise via adversarial training to align feature distributions, further improving the robustness of contrastive learning for ECG signals. GNN-based approaches, like CoLA [23], capture embeddings from high-dimensional attributes and local structures, and ECG-KG [24] vectorizes abnormal triples for improved classification. However, these methods lack clinical knowledge guidance, limiting the understanding of higher-order physiological or pathological relationships between leads and disease labels.

## **2.3 ECG Multimodal Joint Learning**

Inspired by the significant success of multimodal joint learning in natural language processing and computer vision, several ECG diagnostic studies have begun to explore multimodal fusion for representation learning. For instance, IFM [25] generates three types of ECG images—Gramian Angular Field (GAF), Recurrence Plot (RP), and Markov Transition Field (MTF)—to fuse them for heartbeat classification. Similarly, multimodal fusion of ECG and photoplethysmogram (PPG) signals based on wavelet transform has been designed to improve heartbeat detection. However, these methods primarily focus on modality data derived from collection techniques, while professional artificial knowledge, such as clinical reports, remains underutilized. Unlike the remarkable progress in joint learning between medical images and clinical reports [26], the integration of expert knowledge to guide ECG model learning requires further exploration.

## **2.4 ECG Zero-Shot Classification**

Zero-shot classification classifies unseen categories via cross-modal alignment to mitigate data scarcity. However, ECG zero-shot classification demands further research due to discrepancies between ECG signals and radiology reports. MERL [15] proposed a benchmark with clinical knowledge-enhanced prompt engineering (CKEPE) for ECG disease labels, leveraging large-scale pretraining for zero-shot tasks. FG-CLEP [27] enhances ECG-text alignment through fine-grained waveform recovery and two-stage contrastive pretraining, boosting zero-shot classification and linear probing. Notably, these methods overlook cross-modal topological dependencies between ECG and text embeddings and while GNNs [28] excel at capturing such structural information, their application to ECG zero-shot classification remains underexplored. Additionally, ECG data exhibits severe class imbalance (ultra-minority rare arrhythmias account for <1% in most datasets), yet existing methods lack systematic analysis of rare-class performance and the correlation between class frequency and accuracy, hindering clinical utility.

## **3 Methods**

In this section, we first present the relevant symbols involved in the ECG zero-shot classification task. Then, starting from the design of the MCCGAA encoding layer, we provide a detailed explanation of the associated designs, including the GAFA layer and the loss function, as shown in Fig. 1.

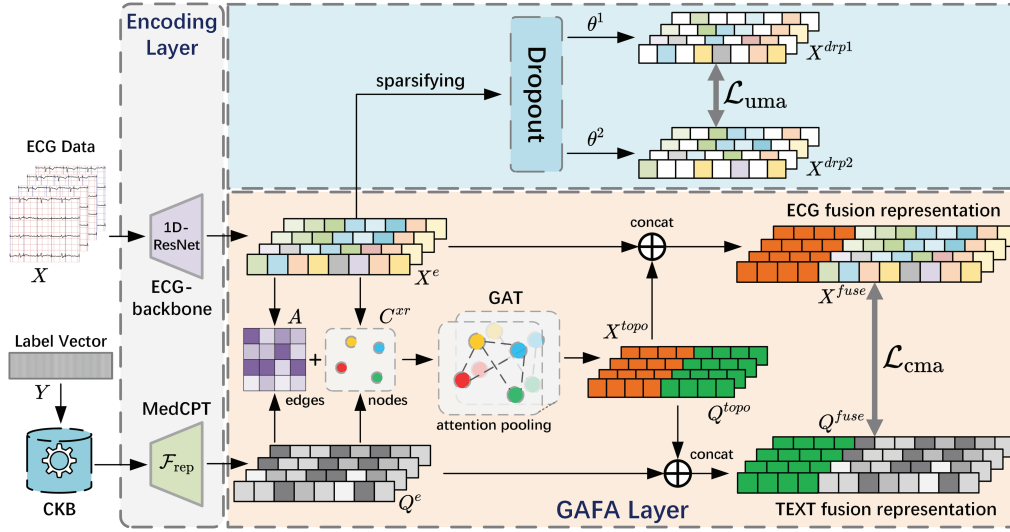


**Figure 1:** Structure diagram of MCCGAA. CKB refers to the Clinical Knowledge Base. For the embedding representations of ECG and clinical reports, on the one hand, both are used to construct a similarity adjacency matrix  $A$  and a dual-embedding graph node set  $C^{xr}$ , which a GAT then processes to capture the topological dependencies between nodes. On the other hand, they are further processed for both unimodal and cross-modal alignment. The symbol  $\oplus$  represents the tensor concatenation operation.

### 3.1 Problem Formulation

The ECG data for  $D$ -lead signals is represented as  $x \in \mathbb{R}^{D \times L}$ , where  $L$  denotes the signal duration. Each sample  $x$  is associated with a label  $y$  indicating a diagnostic category, such as “AFIB” or “VPC”. A collection of  $B$  ECG samples is denoted by  $X = \{x_1, \dots, x_B\}$  with the corresponding label set  $Y = \{y_1, \dots, y_B\}$ . Given a clinical knowledge base  $K = \{k_1, \dots, k_C\}$ , where each  $k_i$  represents the textual report for the  $i$ -th diagnostic category (e.g., “Atrial Fibrillation, Paroxysmal...”), each category in  $Y$  has a unique mapping in  $K$ . The ECG query process is defined as follows:

$$Q = f_{\text{query}}(Y, K) \quad (1)$$

where  $Q = \{r_1, \dots, r_B\}$  represents the diagnostic reports corresponding to  $Y$ . ECG zero-shot classification aims to train a model using a source dataset  $X_s$  and its corresponding query reports  $Q_s$  to minimize their distance in the joint feature space. This knowledge transfer approach enables the model to generalize and classify unseen categories in a separate target dataset.

### 3.2 Encoding Layer

$x$  and  $r$  are two modalities of data that need to be encoded separately for further analysis. In ECG embedding representation learning, to address the crucial role of focusing on a small number of lead signals, we designed a CAM module to improve the attention of 1D-ResNet in the channel dimension. Taking the Block module in Fig. 2 as an example, the  $3 \times 3$  convolution is defined as follows:

$$\chi_i^o = \sum_{j=0}^{k-1} \chi_{i+j} w_j \quad (2)$$

$$x^o = \{\chi_i^o \mid 1 \leq i \leq L\} \quad (3)$$

$$X^o = \{x_i^o \mid 1 \leq i \leq B\} \quad (4)$$

where  $x_{i+j}$  is the element at position  $i + j$  in the input tensor  $x$ ,  $w_j$  is the  $j$ -th weight of the convolutional kernel and  $\chi_i^o$  represents the output value at the  $i$ -th position after convolution. Next, batch normalization (BN) is applied to standardize the output of each layer and reduce internal covariate shift:

$$\hat{X} = \frac{X^o - \mu}{\sigma} \quad (5)$$

$$\hat{X}^o = \gamma \hat{X} + \beta \quad (6)$$

where  $X^o$  is the input to the current layer,  $\mu$  and  $\sigma$  are the mean and standard deviation of the current batch, and  $\gamma$  and  $\beta$  are the learned scaling and shifting parameters. Finally, an activation function is applied to introduce non-linearity into the network:

$$f_{ReLU}(X^o) = \max(0, X^o) \quad (7)$$

if  $X^o$  is greater than or equal to zero,  $f_{ReLU}$  outputs  $X^o$  itself; otherwise, it outputs 0.

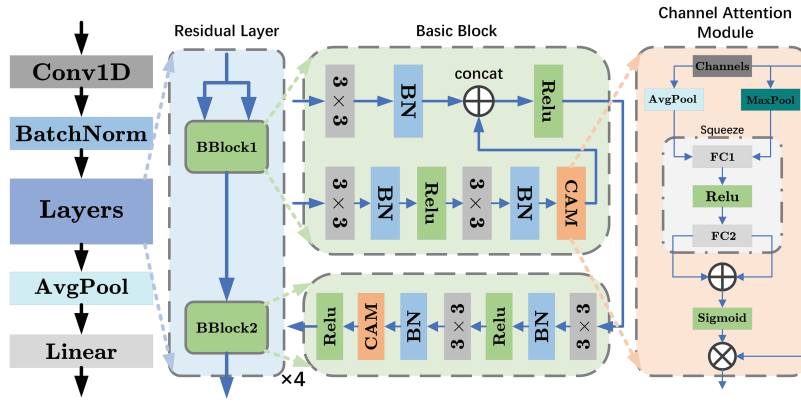


**Figure 2:** Structure diagram of ECG-backbone. The diagram illustrates the design 1D-ResNet18, which consists of four residual layers, each containing two basic blocks. BN represents batch normalization, and  $3 \times 3$  refers to convolutional layers with kernel size 3. ReLU is the activation function. Two types of pooling in CAM (max and average) are used to generate global information from the feature map for further channel attention computation. The squeeze layer performs further transformation and information compression of the features, where the fully connected layer (FC1) compresses the channels to half of the original size, and FC2 does the opposite. The  $\otimes$  represents tensor multiplication.

In the CAM module, both average pooling and max pooling operations are used to capture the global average and maximum information of each channel, thereby learning different contexts of ECG:

$$X^{avg} = f_{AvgPool}(X^o) \quad (8)$$

$$X^{max} = f_{MaxPool}(X^o) \quad (9)$$

Next, two fully connected layers are used to generate the attention weights corresponding to each channel:

$$X_1^{avg} = f_{ReLU}(f_{FC1}(X^{avg})) \quad (10)$$

$$X_1^{max} = f_{ReLU}(f_{FC1}(X^{max})) \quad (11)$$

$$X_2^{avg}, X_2^{max} = f_{FC2}(X_1^{avg}, X_1^{max}) \quad (12)$$

where the number of output channels for  $f_{Fc1}$  is half the number of input channels, while  $f_{Fc2}$  restores it to the original number of input channels. Then, the channel attention scores are summed and mapped to the range  $[0, 1]$ :

$$\alpha = \sigma \left( \frac{1}{1 + e^{-(X_2^{avg} + X_2^{max})}} \right) \quad (13)$$

where  $\sigma$  is the sigmoid activation function, and  $\alpha$  represents the channel attention weights. Finally, the channel attention weights are used to scale the original channel output:

$$X^{CAM} = \alpha \cdot \hat{X}^o \quad (14)$$

The weighted design of the CAM allows the network to adaptively emphasize or suppress features from different channels, thereby improving model performance and capturing the differences in lead signals across various ECG data for different tasks. Furthermore, the output of the 1D-ResNet18 with the integrated CAM module is mapped to the preset embedding vector length by a linear layer:

$$X^e = f_{Linear} (X^{CAM}) \quad (15)$$

where  $X^e \in \mathbb{R}^{B \times M}$ , and  $M$  is the embedding vector length of the ECG.

In ECG diagnostic report embedding representation learning, we used a pre-trained text encoder  $\mathcal{F}_{rep}$  from the medical domain, MedCPT, to generate text embedding vectors. This design allows the task to avoid relying heavily on manual domain knowledge for ECG diagnostic report interpretation, enabling efficient and accurate conversion of complex medical language into structured medical codes:

$$Q^e = \mathcal{F}_{rep} (Q) \quad (16)$$

Prior to similarity calculation, the ECG embedding  $X^e$  undergoes 1D convolution for dimension adjustment, attention-based pooling to aggregate key temporal information into global features, and normalization; the MedCPT text embedding  $Q^e$  is linearly projected via a multi-layer perceptron (MLP) and normalized. Through these operations,  $Q^e$  achieves the same embedding dimension as  $X^e$  ( $Q^e \in \mathbb{R}^{B \times M}$ ), thereby mapping the two modalities into the same semantic space and laying the foundation for subsequent spatial topology-dependent learning.

### 3.3 GAFA Layer

To capture cross-modal topological dependencies between ECGs and diagnostic reports, we propose GAFA, a method based on joint embedding learning of ECG and text representations.

The cross-modal topology in GAFA is modeled as a bipartite graph, where ECG embeddings and diagnostic text embeddings serve as two heterogeneous node types, and edges are constructed based on their pairwise semantic similarity. This formulation enables explicit modeling of ECG–text relational structure, which is subsequently learned via a graph attention network.

With  $X^e$  and  $Q^e$  as inputs, GAFA is defined as:

$$f_{sim}(i, j) = \frac{X_i^e \cdot Q_j^e}{\tau} \quad (17)$$

where  $f_{sim}(i, j)$  represents the similarity between the  $i$ -th ECG embedding and the  $j$ -th diagnostic report under Einstein summation, and  $\tau$  is a scaling factor to stabilize the training process. Next, the threshold adjacency matrix is constructed as follows:

$$A_{ij} = \begin{cases} 1 & \text{if } f_{sim}(i, j) > \text{threshold} \\ 0 & \text{otherwise} \end{cases} \quad (18)$$

where  $A_{ij}$  is an element of the adjacency matrix  $A$ , with a value of 1 indicating an edge between the  $i$ -th ECG embedding and the  $j$ -th diagnostic report, and 0 otherwise. Then,  $X^e$  and  $Q^e$  are used to construct the dual embedding graph nodes further:

$$C^{xr} = X^e \parallel Q^e \quad (19)$$

where  $\parallel$  refers to the tensor concatenation operation.

After the preparation, we use a two-layer multi-head graph attention network (GAT) to capture the spatial topology dependencies between ECG and diagnostic text. The computation for a single-head graph attention layer is as follows:

$$h_i^{(k)} = \sum_{j \in \mathcal{N}(i)} \beta_{ij}^{(k)} C_j^{xr} W^{(k)} \quad (20)$$

where  $\mathcal{N}(i)$  is the set of neighboring nodes of node  $i$ ,  $W^{(k)} \in \mathbb{R}^{2M \times F}$  is the learnable weight matrix for the  $k$ -th attention head,  $F$  is the dimensionality of the output features for each attention head, and  $\beta_{ij}^{(k)}$  is the attention coefficient for the  $k$ -th attention head, representing the attention weight between node  $i$  and its neighboring node  $j$ , which can be computed as follows:

$$\beta_{ij}^{(k)} = \frac{\exp\left(a^{(k)T} \left[ W^{(k)} C_i^{xr} \parallel W^{(k)} C_j^{xr} \right]\right)}{\sum_{s \in \mathcal{N}(i)} \exp\left(a^{(k)T} \left[ W^{(k)} C_i^{xr} \parallel W^{(k)} C_s^{xr} \right]\right)} \quad (21)$$

where  $a^{(k)} \in \mathbb{R}^{1 \times 2H}$  is the learnable weight vector for the  $k$ -th attention head, and  $[W^{(k)} C_i^{xr} \parallel W^{(k)} C_j^{xr}]$  is the concatenated representation of the features of nodes  $i$  and  $j$  after linear transformation.

Finally, we concatenate the outputs of the multiple attention heads to obtain the output of a single-layer GAT:

$$H = (h_1 \parallel h_2 \parallel \dots \parallel h_N) W_O \quad (22)$$

where  $W_O \in \mathbb{R}^{HN \times F}$  is a learnable output weight matrix,  $N$  is the number of attention heads and  $H \in \mathbb{R}^{B \times F}$  is the multi-head attention output of a single-layer GAT. After GAT captures the spatial topology dependencies, we split  $H$  to obtain the dependent embedding representations  $X^{topo}$  and  $Q^{topo}$  for ECG and diagnostic text, respectively. These are then concatenated with  $X^e$  and  $Q^e$  to obtain the fused representations:

$$(X^{topo} \parallel Q^{topo}) = H \quad (23)$$

$$(X^{fuse}, Q^{fuse}) = (X^{topo} \parallel X^e, Q^{topo} \parallel Q^e) \quad (24)$$

where  $X^{fuse}$  and  $Q^{fuse}$  are the fused embedding representations for ECG and diagnostic text, respectively. Finally, these representations will be further used for modality alignment learning.

### 3.4 Modal Alignment Loss Function

A good modal alignment loss function can map the embedding representations of ECG and diagnostic text into a shared space, ensuring that similar or related inputs are closer to each other in this space. Compared to the current clip-style loss function design, the log-sum-exp design offers stronger numerical stability when handling large-scale datasets. To improve the loss function, we propose the following log-sum-exp-based ECG zero-shot classification loss function design:

$$X', Q' = \left( \frac{X^{fuse}}{\|X^{fuse}\|_2}, \frac{Q^{fuse}}{\|Q^{fuse}\|_2} \right) \quad (25)$$

where  $X' \in \mathbb{R}^{B \times (M+F//2)}$  and  $Q' \in \mathbb{R}^{B \times (M+F//2)}$  are the normalized representations, and  $\|X^{fuse}\|_2$  and  $\|Q^{fuse}\|_2$  represent the corresponding euclidean norms. Next, the similarity and log-probability are calculated as follows:

$$f_{sim}^{xq}(i, j) = \left( \frac{\sum_{l=1}^{M+F//2} X'_{i,l} Q'_{j,l}}{\tau} \right) \quad (26)$$

$$f_{prob}^{xq}(i, j) = f_{sim}^{xq}(i, j) - \log \left( \sum_{b=1}^B \exp(f_{sim}^{xq}(i, b)) \right) \quad (27)$$

where  $X'_{i,l}$  represents the value of the  $l$ -th embedding vector of the  $i$ -th ECG sample, and  $Q'_{j,l}$  is similar.  $f_{prob}^{xq}(i, j)$  is the log-probability calculated based on the log-sum-exp trick. Then, we define  $loss_{r2x}$  and  $loss_{x2r}$  as the two loss functions: one for the diagnostic report to ECG and the other for ECG to diagnostic report.

$$loss_{x2r} = -\frac{1}{B} \sum_{i=1}^B f_{prob}^{xq}(i, i) \quad (28)$$

$$loss_{r2x} = -\frac{1}{B} \sum_{i=1}^B f_{prob}^{xq}(i, i)^T \quad (29)$$

$$loss_{all}(X, Q) = loss_{x2r} + loss_{r2x} \quad (30)$$

where  $loss_{x2r}$  represents the log-probability of each ECG embedding and the corresponding diagnostic report embedding at the respective index,  $loss_{r2x}$  represents the log-probability in the opposite direction, and  $loss_{all}$  is the overall loss optimization function.

Notably, the proposed cross-modal alignment is symmetric. Both ECG-to-text and text-to-ECG alignments are optimized using the same similarity matrix, and the final objective is defined as the unweighted sum of the two directional losses. This symmetric design encourages bidirectional embedding alignment in a shared latent space and improves the generalization ability of zero-shot ECG classification.

Finally, considering issues such as errors introduced during the preprocessing of ECG time series, some unimodal embedding regularization methods are used to constrain the model learning. Combined with cross-modal alignment, as shown follows:

$$X^{drp1}, X^{drp2} = f_{Dropout}(X^e, \theta^1, \theta^2) \quad (31)$$

$$\mathcal{L}_{uma}, \mathcal{L}_{cma} = (loss_{all}(X^{drp1}, X^{drp2}), loss_{all}(X, Q)) \quad (32)$$

where  $f_{Dropout}$  represents the regularization layer,  $\theta^1$  and  $\theta^2$  represent different pooling rates,  $\mathcal{L}_{cma}$  represents the cross-modal alignment loss, and  $\mathcal{L}_{uma}$  represents the unimodal alignment loss. After pretraining, MCCGAA can perform zero-shot classification on a new dataset without further training. Specifically, the

query report embeddings corresponding to the total category labels of the new dataset are generated, and the ECG to be classified is encoded using the pre-trained ECG backbone embedding. A simple linear layer is then used to obtain the predicted label directly. Then, accuracy and other evaluation metrics can be calculated based on this.

## 4 Experiments

In this section, extensive experiments are conducted to comprehensively evaluate the performance of MCCGAA. First, seven benchmark datasets, including the pretraining dataset MIMIC-ECG [29], are introduced. Next, the state-of-the-art benchmark methods used for comparison are listed. Several experiments, including linear probing, zero-shot classification, and ablation studies, are then designed to thoroughly examine the interdependencies among different components of MCCGAA. Finally, intuitive feature visualization methods are employed to further analyze the internal mechanisms of MCCGAA, followed by a brief summary. For clarity, the highest value for each dataset is highlighted in bold, and the second-highest value is underlined (“  ”) in the subsequent experimental results tables.

### 4.1 Datasets

To evaluate the performance of MCCGAA, four real-world datasets (PTBXL includes four sub-datasets) were selected. Large-scale pretraining was conducted on MIMIC-ECG, with downstream tasks on CPSC2018 [30], PTBXL [31], and Chapman [32]. Key dataset information is summarized in Table 1.

**Table 1:** Overview of datasets used for zero-shot ECG classification.

Dataset	Samples	Classes	Split (Train/Test/Val)	Key Characteristics
MIMIC-ECG	771,693	47	–	Large-scale multi-center clinical ECG dataset
CPSC2018	6877	9	7:2:1	Real-world clinical ECG recordings with variable length
PTBXL-Form	8978	19	8:1:1	Medium-granularity diagnostic annotations
PTBXL-Sub	21,388	23	8:1:1	Fine-grained diagnostic categories
PTBXL-Super	21,388	5	8:1:1	Coarse-grained diagnostic labels
PTBXL-Rhythm	21,030	12	8:1:1	Rhythm-focused ECG annotations
Chapman	23,026	38	7:2:1	Large-scale multi-class ECG dataset

**Note:** All datasets use standard 12-lead ECG recordings. ECG signals are sampled at 500 Hz and segmented into 10-second windows (5000 sample points), except for CPSC2018, which contains variable-length recordings ranging from 6 to 60 s.

Notably, all datasets exhibit significant class imbalance, consistent with clinical ECG data’s real distribution. Specifically, MIMIC-ECG includes 12 ultra-minority classes (<1%) with dominant classes over 30%; CPSC2018 has 2 ultra-minority classes (e.g., “Other Arrhythmia”) at 0.8%; in the PTBXL series, ultra-minority classes like “Atrial Flutter” (PTBXL-Rhythm) and “Rare Conduction Disorders” (PTBXL-Form) are <0.6%, with only PTBXL-Super (5 classes) showing relative balance; Chapman has a severe long-tailed distribution, with 18 ultra-minority classes (<1%) and top 5 dominant classes making up over 60%. This imbalance poses key challenges for zero-shot classification: models tend to favor dominant classes, fail to

learn rare classes' discriminative features, and traditional contrastive loss is prone to gradient vanishing, worsening unseen rare class classification.

Datasets without official partitions adopt a 7:2:1 train-test-validation split. All models were trained for 20 epochs using the AdamW optimizer with an initial learning rate of  $1.0 \times 10^{-3}$ , cosine-annealed to  $1.0 \times 10^{-8}$ . Experiments were conducted on a Linux server using PyTorch 2.1 with six NVIDIA L20 GPUs (48 GB each).

## 4.2 Baselines

In this experiment, we selected several representative contrastive learning methods as baselines for comparison. To ensure fairness, we implemented all methods using the optimal designs from their original papers. A brief description of each method is provided below:

1. **SimCLR [8]**: A simple and effective contrastive learning framework that learns visual representations through data augmentation and contrastive loss.
2. **BYOL [33]**: A self-supervised method that eliminates negative samples by using a target network to guide representation learning.
3. **BarlowTwins [34]**: A redundancy-reduction learning approach that avoids negative samples while achieving strong performance across vision tasks.
4. **MoCo-v3 [35]**: The first self-supervised framework enabling effective Vision Transformer training with stronger augmentations and longer training schedules.
5. **SimSiam [7]**: A simplified architecture that achieves competitive performance in self-supervised learning without relying on negative pairs.
6. **TS-TCC [6]**: A time-series contrastive learning method that enhances temporal and contextual representation quality without labeled data.
7. **CLOCS [9]**: A contrastive framework across time, space, and patients, enabling robust ECG representations resilient to inter-patient variability.
8. **ASTCL [22]**: An adversarial spatiotemporal contrastive learning method that improves ECG classification and anomaly detection.
9. **CRT [7]**: A self-supervised framework integrating cross-reconstruction and Transformer models to learn high-quality time-series representations.
10. **ST-MEM [10]**: A masked representation learning framework for ECG signals that captures spatiotemporal dependencies via masked prediction.
11. **MERL [15]**: A recent ECG contrastive learning baseline leveraging clinical knowledge prompts to achieve state-of-the-art zero-shot performance.

The receiver operating characteristic (ROC) curve was used to evaluate the effectiveness of the proposed method, as defined by the following formula:

$$\text{AUC} = \sum_{i=1}^{n-1} \frac{\text{TPR}_i + \text{TPR}_{i+1}}{2} \cdot (\text{FPR}_{i+1} - \text{FPR}_i) \quad (33)$$

where  $\text{TPR}_i$  and  $\text{FPR}_i$  represent the true positive rate and the false positive rate at the  $i$ -th point, respectively, and  $n$  is the number of points on the ROC curve. The AUC value is the area under the ROC curve, ranging from 0 to 1, and represents the overall classification performance of the model.

## 4.3 Zero-Shot Learning

In this subsection, we evaluate MCCGAA under a cross-dataset zero-shot generalization scenario to validate the transferability of the knowledge learned on the pre-training MIMIC-ECG dataset to completely

unseen external clinical environments. The detailed characteristics of the benchmark datasets and the specific extent of class imbalance are summarized in Table 1. First, we present the pre-training results of MCCGAA under two different loss function designs, as shown in Fig. 3.

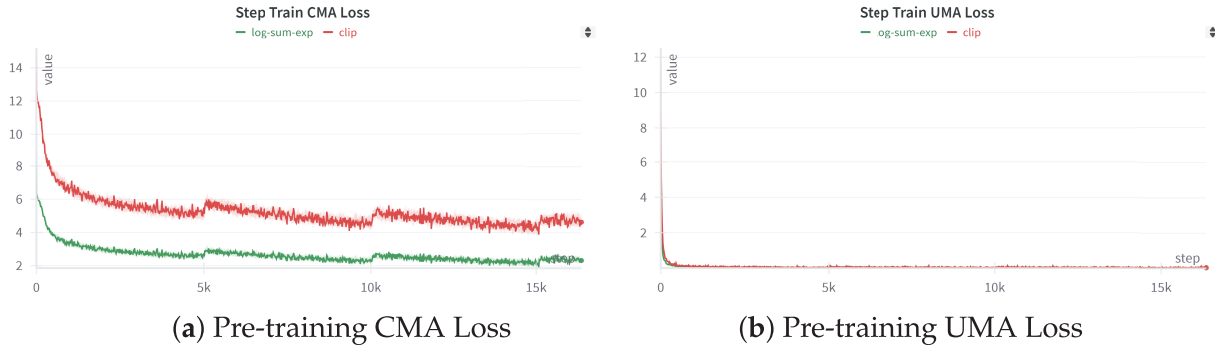


**Figure 3:** MCCGAA’s pretraining step loss function. Apart from the difference in the loss function, the training process and other designs of MCCGAA remain consistent.

Figure (a) illustrates the iteration of the MCCGAA pretraining cross-modal loss. The log-sum-exp design results in a lower loss than the clip method, demonstrating better convergence. Figure (b) shows the iteration of the MCCGAA ECG regularization layer’s unimodal loss. In contrast to Figure (a), the unimodal loss exhibits better convergence, with the loss nearing equilibrium around the 0-step mark. Similarly, the log-sum-exp design continues to show superior performance.

We evaluate zero-shot ECG classification performance using AUROC, which is threshold-independent and robust to severe class imbalance. The results are summarized in Table 2.

**Table 2:** Zero-shot classification results. “N” indicates non-zero-shot classification, using 1% of the training data, while “Y” indicates direct zero-shot classification capability.

Method	Zero-Shot	CPSC2018	PTBXL-Form	PTBXL-Sub	PTBXL-Super	PTBXL-Rhythm	Chapman
Random Init	N	54.96	55.82	55.82	70.45	46.26	47.22
SimCLR	N	59.78	54.98	60.84	63.41	51.41	59.02
BYOL	N	60.88	48.73	57.16	71.70	41.99	54.20
BarlowTwins	N	55.12	52.12	62.57	72.87	50.12	60.72
MoCo-v3	N	62.13	50.32	55.88	73.19	51.38	54.61
SimSiam	N	58.35	55.16	62.52	73.15	49.30	58.25
TS-TCC	N	57.07	48.04	53.54	70.73	43.34	55.26
CLOCS	N	59.59	51.97	57.94	68.94	47.19	54.38
ASTCL	N	57.90	44.14	61.86	72.51	52.38	56.40
CRT	N	58.01	46.41	61.98	69.68	47.44	56.21
ST-MEM	N	56.69	55.71	54.12	61.12	51.12	59.77
MERL	Y	<u>82.80</u>	<u>65.92</u>	<u>75.66</u>	<u>74.26</u>	<u>78.56</u>	<u>74.45</u>
MCCGAA	Y	<b>84.12 ±</b>	<b>68.47 ±</b>	<b>77.37 ±</b>	<b>75.63 ±</b>	<b>84.01 ±</b>	<b>76.41 ±</b>
(Ours)		<b>0.55</b>	<b>0.42</b>	<b>0.50</b>	<b>0.48</b>	<b>0.68</b>	<b>0.47</b>

In the zero-shot classification stage, this study strictly follows a cross-dataset zero-shot generalization protocol. Non-zero-shot baselines were evaluated using 1% of the training data, whereas MCCGAA was pre-trained exclusively on MIMIC-ECG and directly evaluated on six external public datasets without any downstream fine-tuning. This setup rigorously tests the model’s ability to generalize to unseen data distributions and different clinical institutions. MCCGAA achieves competitive performance across most downstream tasks. The relatively lower AUC on PTBXL-Super can be attributed to the limited number of samples in this dataset, which constrains the ability of zero-shot models to generalize effectively to unseen classes.

A detailed comparison with MERL, as summarized in [Table 2](#), shows that MCCGAA consistently outperforms MERL across all datasets, yielding an average AUC improvement of 2.37%. The largest gain is observed on PTBXL-Rhythm, with the AUC increasing from 78.56% to 84.59%.

The PTBXL-Rhythm dataset exhibits a highly imbalanced distribution, where a few common rhythm classes dominate most samples while several rare classes constitute less than 1%, posing challenges for robust feature learning. It focuses on rhythm abnormality classification, placing high demands on cross-modal semantic alignment between ECG representations and textual disease descriptions. Ultra-minority classes such as Atrial Flutter account for only 0.5% of samples, making discriminative feature learning difficult without strong semantic guidance.

MERL primarily relies on convolutional ECG encoders and CLIP-style contrastive alignment, which lack an explicit cross-modal topological structure to enforce structured correspondence between ECG embeddings and textual concepts. Under extreme data scarcity, this may lead to fragmented or weak alignment for rare rhythm classes.

In contrast, MCCGAA introduces the GAFA layer to explicitly construct a cross-modal topology between ECG and text embeddings, enabling structured semantic interaction and robust alignment even for ultra-minority categories. Meanwhile, CAM adaptively highlights diagnostically relevant ECG leads, complementing the cross-modal alignment by enhancing signal quality at the representation level. Together, these mechanisms mitigate the impact of sample scarcity and lead to a 6.03% AUC improvement on PTBXL-Rhythm.

#### 4.4 Linear Probing Fine-Tuning

In this subsection, we use the linear probing technique to validate the transfer learning capability of MCCGAA in order to demonstrate the necessity of MCCGAA’s pre-training. Specifically, we freeze most of the layers in MCCGAA and retain only a simple linear layer as the classifier for learning. This operation allows us to preserve as many of the ECG features learned by MCCGAA during the pre-training phase as possible, which are then used for downstream dataset classification. To further emphasize the importance of knowledge transfer learning, we set three levels of downstream task training dataset proportions: 1%, 10%, and 100%. It allows the model to exhibit different learning abilities with varying data distributions at different training data proportions. The experimental results are shown in [Table 3](#).

**Table 3:** MCCGAA’s linear probing AUC evaluation on six real-world datasets.

Method	CPSC2018			Chapman			PTBXL-Rhythm			PTBXL-Super			PTBXL-Form			PTBXL-Sub		
	1%	10%	100%	1%	10%	100%	1%	10%	100%	1%	10%	100%	1%	10%	100%	1%	10%	100%
SimCLR	59.78	68.52	76.54	59.02	67.26	73.20	51.41	69.44	77.73	63.41	69.77	73.53	54.98	56.97	62.52	60.84	56.97	73.39
BYOL	60.88	74.42	78.75	54.20	71.92	74.69	41.99	74.40	77.17	71.70	73.83	76.45	48.73	61.63	70.82	57.16	61.63	71.64
BarlowTwins	55.12	72.75	78.39	60.72	71.64	77.43	50.12	73.54	77.62	72.87	75.96	78.41	52.12	60.39	66.14	62.57	60.39	74.34

(Continued)

Table 3 (continued)

Method	CPSC2018			Chapman			PTBXL-Rhythm			PTBXL-Super			PTBXL-Form			PTBXL-Sub		
	1%	10%	100%	1%	10%	100%	1%	10%	100%	1%	10%	100%	1%	10%	100%	1%	10%	100%
MoCo-v3	62.13	76.74	75.29	54.61	74.26	77.68	51.38	71.66	74.33	73.19	76.65	78.26	50.32	63.71	71.31	55.88	63.71	76.69
SimSiam	58.35	72.89	75.31	58.25	68.61	77.41	49.30	69.47	75.92	73.15	72.70	75.63	55.16	62.91	71.31	62.52	62.91	76.38
TS-TCC	57.07	73.62	78.72	55.26	68.48	76.79	43.34	69.48	78.23	70.73	75.88	78.91	48.04	61.79	71.18	53.54	61.79	77.87
CLOCS	59.59	77.78	77.49	54.38	71.93	76.13	47.19	71.88	76.31	68.94	73.36	76.31	51.97	57.96	72.65	57.94	57.96	76.24
ASTCL	57.90	77.01	79.51	56.40	70.87	75.79	52.38	71.98	76.05	72.51	77.31	81.02	44.14	60.93	66.99	61.86	60.93	76.51
CRT	58.01	76.43	82.03	56.21	73.70	78.80	47.44	73.52	74.41	69.68	78.24	77.24	46.41	59.49	68.73	61.98	59.49	78.67
ST-MEM	56.69	63.32	70.39	59.77	66.87	71.36	51.12	65.44	74.85	61.12	66.87	71.36	55.71	59.99	66.07	54.12	59.99	63.59
MERL	<u>70.33</u>	<b>85.32</b>	<u>90.57</u>	<b>66.60</b>	<u>82.74</u>	<u>87.95</u>	<u>53.33</u>	<u>82.88</u>	<u>88.34</u>	<b>82.39</b>	<b>86.27</b>	<u>88.67</u>	<b>58.26</b>	<b>72.43</b>	<u>79.65</u>	<u>64.90</u>	<u>80.56</u>	<u>84.72</u>
MCCGAA (Ours)	<b>70.54</b>	<u>81.29</u>	<b>93.75</b>	<u>64.27</u>	<b>85.48</b>	<b>94.00</b>	<u>61.57</u>	<b>85.79</b>	<b>93.36</b>	<u>78.73</u>	<u>86.04</u>	<b>90.70</b>	<u>55.95</u>	<u>71.00</u>	<b>80.01</b>	<b>69.90</b>	<b>81.38</b>	<u>87.77</u>

The experiment shows that MCCGAA achieves good evaluation results on most datasets. With a 100% training sample ratio, some datasets experience a significant performance improvement, such as Chapman and PTBXL-Rhythm. Also, relatively good evaluation results are obtained even with a 10% training sample ratio. It is worth noting that the accuracy is lower on the PTBXL-Super and PTBXL-Form datasets, likely due to the fewer categories, making it more difficult for the model to learn this coarse-grained data distribution from the knowledge pre-trained on large datasets, reflecting a domain-specific preference in transfer learning.

Combined with the analysis of dataset scales, the performance patterns of the MCCGAA are clearly observable:

- 1% training data: For small-sample datasets (e.g., CPSC2018 [6877 samples], PTBXL-Form [8978 samples]), performance is notably constrained at 1% data ratio. Larger datasets are less impacted by scarcity. Via pre-trained ECG features, MCCGAA mitigates small-sample shortcomings while outperforming most baselines on larger datasets, highlighting pre-trained features' universal compensatory value across scales.
- 10% training data: With moderate training data, small-sample datasets' (CPSC2018, PTBXL-Form) limitations are greatly reduced, performance converging to other datasets. All collectively reach stable performance, with medium/large datasets showing more robust improvements due to foundational data advantages. This confirms combining pre-trained features with moderate data amplifies transfer learning effectiveness.
- 100% training data: With full training data, MCCGAA performs excellently across all datasets. Even CPSC2018/PTBXL-Form (small-sample) overcome bottlenecks via pre-trained features integrated with full task-specific data. Large datasets (e.g., Chapman) show more pronounced advantages via deep feature-sample adaptation, validating pre-training maximizes transfer learning for diverse scales.

In summary, the performance of MCCGAA is jointly affected by training sample proportion and dataset scale: it is sensitive to category complexity in small-sample scenarios, and its performance improves significantly with increasing data volume. This confirms its strong pre-trained feature representation and transfer learning capabilities.

#### 4.5 Ablation Experiments

In this subsection, we focus on the interactions and self-stability between different layers of MCGAA. Specifically, we demonstrate the dependencies among various modules of MCGAA by replacing or removing the corresponding designs. The experimental design details are as follows:

- MCGAA w/o GAT attention aggregation: We remove the GAT layer design, directly align ECG and report embeddings across modalities, and then evaluate the zero-shot classification performance under this condition.
- MCGAA w/o log-sum-exp: We replace MCGAA’s log-sum-exp design with the CLIP-style loss function and evaluate the zero-shot classification performance under this condition.
- MCGAA w/o CAM: We remove the CAM channel compression attention design and replace it with the original 1D-ResNet18 design, then evaluate the zero-shot classification performance under this condition.

The ablation results are summarized in Table 4. Removing different components leads to varying degrees of performance degradation across datasets, indicating that each module contributes to MCGAA through distinct mechanisms.

**Table 4:** Ablation experiment. “w/o” stands for “without”, and “avg AUC” refers to the average AUC classification accuracy.

Ablation Design	CPSC2018	PTBXL-Form	PTBXL-Sub	PTBXL-Super	PTBXL-Rhythm	Chapman
MCGAA	<b>84.35</b>	<u>68.81</u>	<u>77.51</u>	75.75	<b>84.59</b>	<b>76.69</b>
w/o GAT	81.32	66.80	<b>77.80</b>	<b>78.71</b>	<u>82.44</u>	<u>75.71</u>
w/o log-sum-exp	82.29	<b>69.44</b>	77.30	73.43	80.87	74.98
w/o CAM	82.46	68.55	76.65	<u>77.66</u>	80.29	75.52
avg AUC	82.61	68.40	77.32	76.39	82.05	75.73

The GAT attention aggregation module models cross-modal topological relationships between ECG and text embeddings. Its removal causes moderate performance drops on datasets with few samples or rare classes, such as CPSC2018, where the AUC decreases by 3.03 points. On most rhythm or multi-class datasets, the decrease is smaller than that observed when removing CAM or replacing the log-sum-exp loss. This suggests that GAT primarily refines cross-modal alignment rather than directly improving feature quality. It can be reasonably inferred that cross-modal topological modeling helps mitigate alignment difficulties for rare-class samples when data is scarce.

The log-sum-exp loss stabilizes gradients and governs the geometry of the embedding space. Replacing it with a CLIP-style loss leads to pronounced AUC drops on imbalanced datasets, e.g., PTBXL-Rhythm, where AUC decreases from 84.59 to 80.87, and Chapman, where AUC decreases from 76.69 to 74.98; the effect is smaller on PTBXL-Super, decreasing from 75.75 to 73.43. This indicates that log-sum-exp provides smoother gradients for scarce rare-class samples, maintaining stable contrastive learning. It can be reasonably inferred that this loss alleviates the masking of rare-class features by dominant-class gradients, thereby enhancing zero-shot classification performance.

The CAM module enhances ECG embeddings via adaptive channel compression and lead-wise attention. Its removal results in the largest performance drop on PTBXL-Rhythm, where AUC decreases from 84.59 to 80.29, and notable decreases on CPSC2018 (from 84.35 to 82.46) and Chapman (from 76.69 to

75.52). This highlights CAM’s role in improving signal quality before cross-modal alignment, particularly in emphasizing critical leads for rare classes and suppressing noise. It can be reasonably inferred that CAM facilitates the extraction of discriminative features for rare classes, which explains the significant performance decline when removed.

For PTBXL-Super, which contains a small number of relatively balanced classes, certain ablations (e.g., w/o GAT) do not substantially reduce performance and may even slightly improve it (78.71 vs. 75.75). This suggests that under balanced conditions, the marginal contribution of higher-level modules is limited, and removing some modules may reduce over-parameterization, allowing the model to focus on robust, coarse-grained discriminative features.

In summary, the components of MCCGAA contribute at different stages of representation learning: CAM and the log-sum-exp loss primarily enhance feature quality and embedding stability, whereas GAT provides complementary gains through cross-modal topology. Combined with large-scale pretraining on MIMIC-ECG, these modules enable MCCGAA to achieve robust zero-shot classification performance across diverse downstream datasets. It can be reasonably inferred that these modules play a key role in mitigating rare-class scarcity and class imbalance.

#### 4.6 Parameter Stability

To further assess the impact of different designs, in keeping other designs unchanged, we evaluated the effect of four basic architectures, ResNet18, ResNet34, ResNet50, and ResNet101, on the ECG feature extraction backbone network. Specifically, we integrated the different architectures using the CAM module, then pre-trained the MCCGAA based on this, and finally evaluated the benchmark dataset in a zero-shot classification task. The results are shown in [Table 5](#):

**Table 5:** Evaluation of ECG-backbone with different architectures on six benchmark datasets.

ECG-backbone	CPSC2018	PTBXL-Form	PTBXL-Sub	PTBXL-Super	PTBXL-Rhythm	Chapman	Avg. AUC
1D-ResNet18	<b>84.35</b>	<b>68.81</b>	<u>77.51</u>	75.75	<b>84.59</b>	<b>76.69</b>	<b>77.95</b>
1D-ResNet34	<u>79.86</u>	<u>65.43</u>	77.18	<b>78.55</b>	<u>82.94</u>	<u>75.38</u>	<u>76.56</u>
1D-ResNet50	74.97	60.96	74.54	75.68	78.37	72.03	72.76
1D-ResNet101	78.63	64.11	<b>77.68</b>	<u>76.64</u>	77.13	72.28	74.41
avg AUC	79.45	64.83	76.73	76.66	80.76	74.10	75.42

Overall, the 1D-ResNet18 exhibited the highest average AUC, reaching 77.95. On the one hand, as the complexity of the ECG architecture increased, the accuracy across six datasets showed varying degrees of decline. On the other hand, it is worth noting that increasing network complexity led to an accuracy improvement in some datasets, such as PTBXL-Form and PTBXL-Super. The above experimental results suggest that while increasing the complexity of the ECG backbone network may lead to a decline in evaluation accuracy, this overfitting issue seems to be offset by capturing more features, resulting in a certain accuracy improvement. However, more parameters are needed to capture more complex patterns.

In addition to the above discussion, we also designed experiments to evaluate the stability of the embedding vector representation for GAT, as shown in [Table 6](#). The dimensions of the hidden layers were set to 1/4, 1/2, and 2 times the original embedding vector length, with the output layer length being half of the corresponding hidden layer. Similar to the ECG feature extraction backbone, the results showed

that as the hidden layer dimensions increased, some datasets exhibited an AUC that initially increased and then decreased. Furthermore, as the degree of overfitting increased, the datasets generally showed a decline in accuracy, suggesting that high-dimensional hidden layers overly complicate the capture of topological dependencies. However, the design with hidden layer dimensions set to 1/2 achieved relatively good evaluation results.

**Table 6:** Evaluation of GAT with different architectures on six benchmark datasets.

(Hidden, output)	CPSC2018	PTBXL-Form	PTBXL-Sub	PTBXL-Super	PTBXL-Rhythm	Chapman	Avg. AUC
(32, 16)	82.66	67.85	76.73	<b>78.75</b>	<u>82.94</u>	<b>79.06</b>	<b>78.00</b>
(64, 32)	<b>84.35</b>	<b>68.81</b>	<b>77.51</b>	75.74	<b>84.58</b>	<u>76.68</u>	<u>77.95</u>
(128, 64)	<u>82.75</u>	<u>68.23</u>	<u>77.27</u>	<u>78.22</u>	81.34	75.62	77.24
(256, 128)	80.31	66.99	75.62	75.82	80.11	75.79	75.77
avg AUC	82.52	67.97	76.78	77.13	82.24	76.79	77.24

#### 4.7 Feature Visualization

In this subsection, we analyze the internal working mechanism of MCCGAA from the perspective of feature representation and data flow, aiming to provide an intuitive explanation of how different components contribute to zero-shot classification. We employ t-SNE to visualize the distribution of learned embeddings, which is widely used to qualitatively assess the clustering structure of high-dimensional representations. The t-SNE visualizations of six public datasets are shown in Fig. 4.

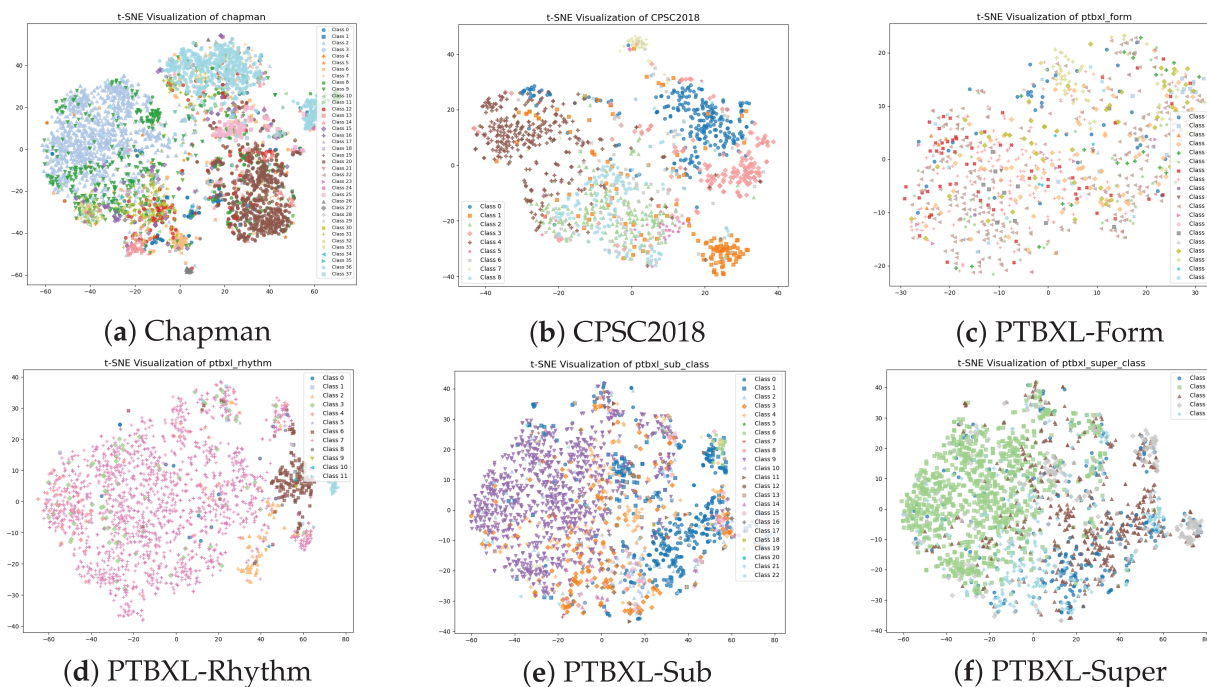


**Figure 4:** t-SNE visualization of the dataset. The zero-shot classification visualization of MCCGAA on six public datasets shows that the closer the samples of the same class are, the better the classification performance.

As shown in Fig. 4, MCCGAA projects high-dimensional ECG representations into a low-dimensional space where samples from the same category tend to form compact local clusters, while different categories remain relatively separable. This clustering behavior is more evident for classes with relatively sufficient samples, indicating that MCCGAA effectively captures discriminative semantic structures during pretraining and cross-modal alignment.

In contrast, categories with fewer samples generally exhibit weaker clustering behavior. Under pronounced data imbalance, minority classes tend to be scattered or partially overlapped with other categories in the embedding space. This suggests that limited sample availability constrains the model's ability to learn representative semantic patterns for these classes during pretraining, leading to increased ambiguity in the learned feature space. While MCCGAA achieves robust zero-shot discrimination on most datasets, its performance on small-sample categories (e.g., PTBXL-Form) indicates potential room for improvement in mitigating class imbalance during representation learning.

To further analyze the working principles of MCCGAA, we investigate the dependency between ECG signals and clinical reports at the embedding level. An example from the PTBXL-Rhythm dataset is used to visualize the learned ECG embedding, as shown in Fig. 5.

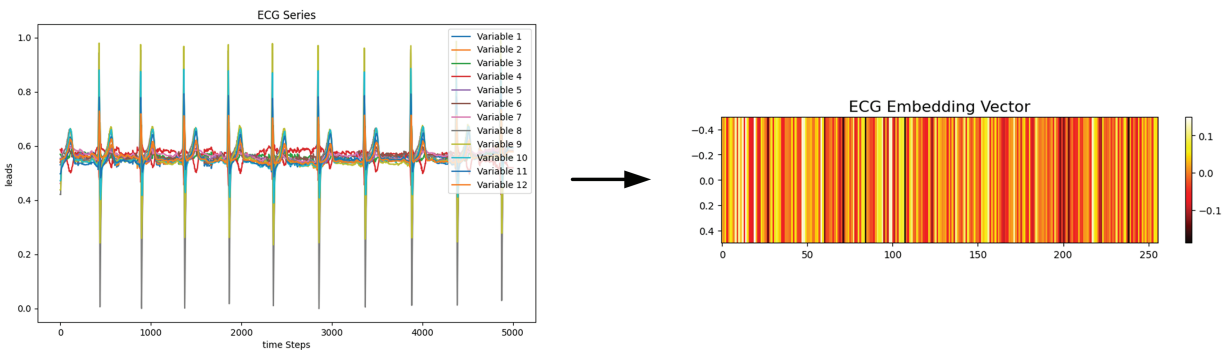


**Figure 5:** A single ECG sample and its corresponding embedding vector. The ECG sequence with 12 variables is encoded into a 256-dimensional vector, where different color bands in the embedding vector represent distinct feature representations.

The ECG signal is encoded into a 256-dimensional embedding vector exhibiting structured and non-random patterns across dimensions, suggesting that the encoder captures meaningful temporal and morphological characteristics of ECG signals.

Subsequently, we examine the relationship between ECG embeddings and clinical report embeddings by computing their similarity through tensor multiplication, as shown in Fig. 6. Both ECG and clinical report embeddings exhibit consistent structural patterns, and the resulting correlation heatmap shows that ECG embeddings achieve higher similarity with their corresponding clinical categories than with unrelated reports. These results demonstrate that MCCGAA aligns ECG signals and clinical reports in a shared semantic space, enabling zero-shot classification based on embedding similarity rather than explicit label supervision.

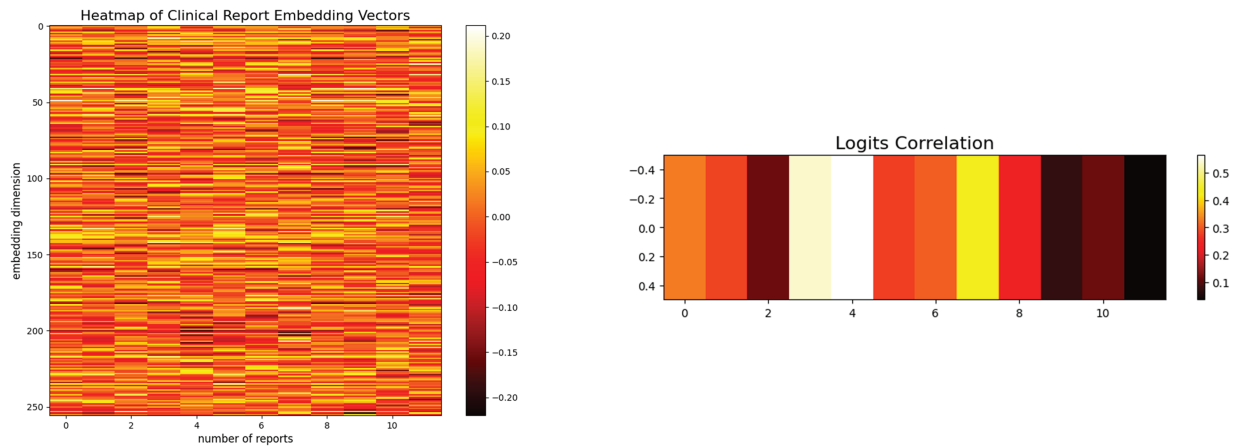


**Figure 6:** The heatmap of the 256-dimensional embedding representations for 12 clinical reports and their corresponding logits correlation vectors. A stronger logit correlation results in a more vivid color band for the clinical report, while a weaker correlation leads to a less vibrant color.

To further account for the topological correlation between ECG samples and textual reports, Fig. 7 illustrates their dynamic association, which quantifies the similarity between ECG signals and diagnostic texts. The numerical values within the red squares denote the GAT attention weights. The evolution of GAT attention heatmaps in this figure reveals a dynamic alignment process, shifting from diffuse exploration to precise focusing. At the initial stage (Epoch 4), the attention weights remain low ( $\approx 0.05$ ) and scattered, indicating weak cross-modal specificity. By Epoch 10, the peak intensity triples to 0.16, demonstrating that the GAFA layers effectively amplify critical diagnostic signals while suppressing cross-modal noise.

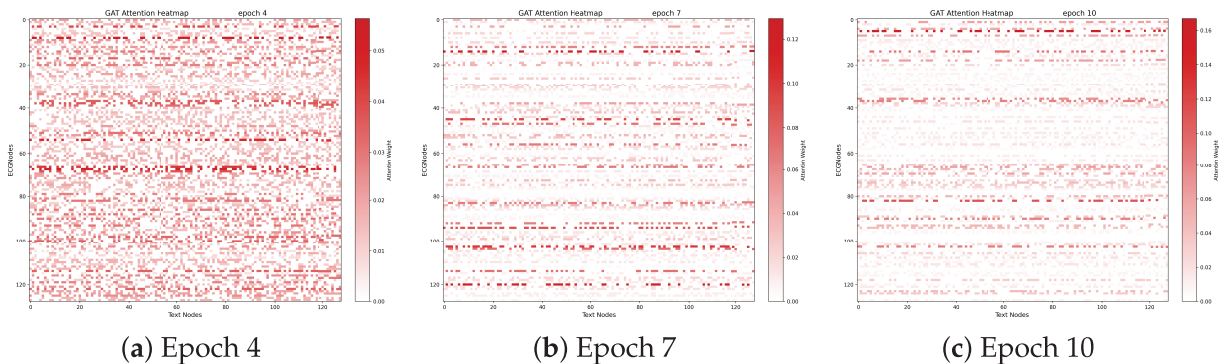


**Figure 7:** Evolution of GAT attention heatmaps across different training stages. As training progresses from (a) to (c), the attention patterns become increasingly sparse and focused, which visualizes the strengthened spatial topological correlation between ECG signals and textual reports and indicates that the GAFA layer effectively learns to prioritize pivotal diagnostic segments while suppressing modal noise.

The resulting structural sparsity and prominent horizontal “resonance” bands signify the formation of diagnostic anchors. Specifically, specific ECG morphological nodes consistently govern multiple semantic tokens, mimicking the clinical reasoning paradigm where a single waveform abnormality (e.g., an abnormal QRS complex) underpins multiple diagnostic conclusions. This progressive refinement of the internal graph topology confirms that the GAT mechanism captures the intrinsic logical mappings between ECG features and diagnostic semantics, thereby laying a robust and interpretable foundation for zero-shot classification.

To evaluate the zero-shot prediction behavior of MCGAA at the label level, Fig. 8 illustrates the confusion matrices for three representative categories: ST, RBBB, and AF. For ST, the model exhibits balanced recognition performance with moderate false positives and negatives. Notably, RBBB represents a typical imbalanced category with a significantly low prevalence in the dataset; however, MCGAA demonstrates remarkable robustness, achieving the highest specificity and the smallest overall classification error despite the scarcity of positive samples. In contrast, AF shows a higher false-positive rate, which may be attributed to overlapping ECG morphological characteristics and the inherent label ambiguity often encountered in multi-label clinical datasets.

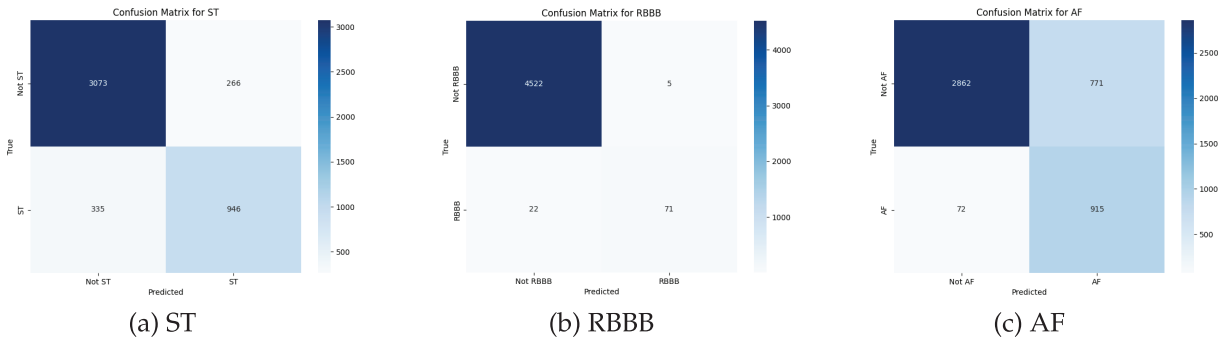


**Figure 8:** Confusion matrices of MCGAA for three representative categories in the Chapman dataset. From left to right: (a) ST-segment abnormality, (b) Right bundle branch block, and (c) Atrial fibrillation. Rows represent true labels and columns represent predicted labels.

## 5 Conclusion

In this paper, we propose a method named MCGAA for ECG zero-shot classification. MCGAA employs a CAM to focus on key lead signals in the design of the ECG feature extraction backbone network, thereby enhancing the learning of ECG embedding representations. For cross-modal alignment, MCGAA introduces a graph attention feature alignment network to capture the spatial topological dependencies between ECG signals and clinical reports, addressing the insufficient representational power in the alignment process. In the design of the loss function, the log-sum-exp function achieves better evaluation accuracy and convergence than the clip-style approach, thus accelerating the pretraining process of MCGAA. Experimental results demonstrate that MCGAA outperforms the latest methods across six public datasets, showing promising potential for improving decision support for ECG zero-shot classification. Furthermore, the robustness and imbalance analyses conducted in this study underscore the model's practical utility in clinical settings. By maintaining stability under complex noise and reliability in identifying ultra-minority arrhythmias (<1%), MCGAA ensures consistent and trustworthy decision support in real-world scenarios characterized by long-tailed data distributions.

However, there are some limitations. On the one hand, MCGAA concatenates the spatial topological dependencies across modalities, which may lead to sparse vectors and an increased risk of overfitting. On the other hand, existing methods for ECG unimodal alignment use dropout layers to generate alignment vectors, but this random dropout of neurons may reduce the model's interpretability. Future work could focus on improving the spatial topological dependency learning between ECG and clinical report embedding vectors and the design of the alignment loss function between them. One potential research direction is to develop more sophisticated and efficient graph neural networks and loss functions.

**Acknowledgement:** Not applicable.

**Funding Statement:** The authors thank the Guizhou Provincial Basic Research Program (Natural Science) for funding this work through Research Group No. QKHJC-ZK(2024)YB062.

**Author Contributions:** The authors confirm contribution to the paper as follows: study conception and design: Qiuxiao Mou; data collection: Qiuxiao Mou, Haoyu Gui; analysis and interpretation of results: Qiuxiao Mou, Haoyu Gui, Xianghong Tang, Jianguang Lu; draft manuscript preparation: Qiuxiao Mou, Haoyu Gui. All authors reviewed and approved the final version of the manuscript.

**Availability of Data and Materials:** The code used in this study is available at <https://github.com/QXMou1/MCCGAA>.

**Ethics Approval:** Not applicable.

**Conflicts of Interest:** The authors declare no conflicts of interest.

## References

1. Geselowitz DB. On the theory of the electrocardiogram. *Proc IEEE*. 1989;77(6):857–76. doi:10.1109/5.29327.
2. Baloglu UB, Talo M, Yildirim O, San Tan R, Acharya UR. Classification of myocardial infarction with multi-lead ECG signals and deep CNN. *Pattern Recogn Lett*. 2019;122:23–30. doi:10.1016/j.patrec.2019.02.016.
3. Lu H, Ong K, Chia P. An automated ECG classification system based on a neuro-fuzzy system. In: *Computers in cardiology 2000*. Vol. 27. Piscataway, NJ, USA: IEEE; 2000. p. 387–90 doi: 10.1109/cic.2000.898538.
4. Kiranyaz S, Ince T, Hamila R, Gabbouj M. Convolutional neural networks for patient-specific ECG classification. In: *2015 37th Annual International Conference of the IEEE Engineering in Medicine and Biology Society (EMBC)*. Piscataway, NJ, USA: IEEE; 2015. p. 2608–11.
5. Hou B, Yang J, Wang P, Yan R. LSTM-based auto-encoder model for ECG arrhythmias classification. *IEEE Trans Instrument Measur*. 2019;69(4):1232–40. doi:10.1109/tim.2019.2910342.
6. Eldele E, Ragab M, Chen Z, Wu M, Kwok CK, Li X, et al. Time-series representation learning via temporal and contextual contrasting. *arXiv:2106.14112*. 2021.
7. Zhang W, Yang L, Geng S, Hong S. Self-supervised time series representation learning via cross reconstruction transformer. *IEEE Trans Neural Netw Learn Syst*. 2024;35(11):16129–38. doi:10.1109/tnnls.2023.3292066.
8. Chen T, Kornblith S, Norouzi M, Hinton G. A simple framework for contrastive learning of visual representations. In: *International Conference on Machine Learning*. London, UK: PMLR; 2020. p. 1597–607.
9. Kiyasseh D, Zhu T, Clifton DA. Clocs: contrastive learning of cardiac signals across space, time, and patients. In: *International Conference on Machine Learning*. London, UK: PMLR; 2021. p. 5606–15.
10. Na Y, Park M, Tae Y, Joo S. Guiding masked representation learning to capture spatio-temporal relationship of electrocardiogram. *arXiv:2402.09450*. 2024.
11. Xie X, Liu H, Shu M, Zhu Q, Huang A, Kong X, et al. A multi-stage denoising framework for ambulatory ECG signal based on domain knowledge and motion artifact detection. *Future Generat Comput Syst*. 2021;116:103–16. doi:10.1016/j.future.2020.10.024.
12. Liu C, Wan Z, Cheng S, Zhang M, Arcucci R. ETP: learning transferable ECG representations via ECG-text pre-training. In: *ICASSP 2024-2024 IEEE International Conference on Acoustics, Speech and Signal Processing (ICASSP)*. Piscataway, NJ, USA: IEEE; 2024. p. 8230–4.
13. Lalam SK, Kunderu HK, Ghosh S, Kumar H, Awasthi S, Prasad A, et al. ECG representation learning with multi-modal EHR data. *Trans Mach Learn Res*. 2023.
14. Huang SC, Pareek A, Jensen M, Lungren MP, Yeung S, Chaudhari AS. Self-supervised learning for medical image classification: a systematic review and implementation guidelines. *npj Digit Med*. 2023;6(1):74. doi:10.1038/s41746-023-00811-0.
15. Liu C, Wan Z, Ouyang C, Shah A, Bai W, Arcucci R. Zero-shot ECG classification with multimodal learning and test-time clinical knowledge enhancement. *arXiv:2403.06659*. 2024.

16. Safarballi B, Golpayegani SMRH. Nonlinear dynamic approaches to identify atrial fibrillation progression based on topological methods. *Biomed Signal Process Control*. 2019;53:101563. doi:10.1016/j.bspc.2019.101563.
17. Scarselli F, Gori M, Tsoi AC, Hagenbuchner M, Monfardini G. The graph neural network model. *IEEE Trans Neural Netw*. 2008;20(1):61–80. doi:10.1109/tnn.2008.2005605.
18. Chen T, Hong R, Guo Y, Hao S, Hu B. MS<sup>2</sup>-GNN: exploring GNN-based multimodal fusion network for depression detection. *IEEE Trans Cybern*. 2022;53(12):7749–59. doi:10.1109/tyb.2022.3197127.
19. Siontis KC, Noseworthy PA, Attia ZI, Friedman PA. Artificial intelligence-enhanced electrocardiography in cardiovascular disease management. *Nature Rev Cardiol*. 2021;18(7):465–78. doi:10.1038/s41569-020-00503-2.
20. Din S, Qaraqe M, Mourad O, Qaraqe K, Serpedin E. ECG-based cardiac arrhythmias detection through ensemble learning and fusion of deep spatial-temporal and long-range dependency features. *Artif Intell Med*. 2024;150:102818. doi:10.1016/j.artmed.2024.102818.
21. Hyvarinen A, Morioka H. Unsupervised feature extraction by time-contrastive learning and nonlinear ICA. In: 30th Conference on Neural Information Processing Systems (NIPS 2016); 2016 Dec 5–10; Barcelona, Spain. p. 1–9.
22. Wang N, Feng P, Ge Z, Zhou Y, Zhou B, Wang Z. Adversarial spatiotemporal contrastive learning for electrocardiogram signals. *IEEE Trans Neural Netw Learn Syst*. 2024;35(10):13845–59. doi:10.1109/tnnls.2023.3272153.
23. Liu Y, Li Z, Pan S, Gong C, Zhou C, Karypis G. Anomaly detection on attributed networks via contrastive self-supervised learning. *IEEE Trans Neural Netw Learn Syst*. 2021;33(6):2378–92. doi:10.1109/tnnls.2021.3068344.
24. Ge Z, Cheng H, Tong Z, He Z, Alhudhaif A, Polat K, et al. A knowledge-driven graph convolutional network for abnormal electrocardiogram diagnosis. *Knowl Based Syst*. 2024;296(1):111906. doi:10.1016/j.knosys.2024.111906.
25. Ahmad Z, Tabassum A, Guan L, Khan N. ECG heart-beat classification using multimodal image fusion. In: ICASSP 2021-2021 IEEE International Conference on Acoustics, Speech and Signal Processing (ICASSP). Piscataway, NJ, USA: IEEE; 2021. p. 1330–4.
26. Radford A, Kim JW, Hallacy C, Ramesh A, Goh G, Agarwal S, et al. Learning transferable visual models from natural language supervision. In: International Conference on Machine Learning. London, UK: PMLR; 2021. p. 8748–63.
27. Liu C, Ding Z, Liu Z, Huang Z. Two-stage contrastive language electrocardiogram pre-training for fine-grained waveform features. In: 1st ICML Workshop on Foundation Models for Structured Data. London, UK: PMLR; 2025. p. 1–10.
28. Dehmamy N, Barabási AL, Yu R. Understanding the representation power of graph neural networks in learning graph topology. In: Advances in neural information processing systems. London, UK: PMLR; 2019.
29. Gow B, Pollard T, Nathanson LA, Johnson A, Moody B, Fernandes C, et al. Mimic-iv-ECG-diagnostic electrocardiogram matched subset (version 1.0). *PhysioNet*. 2023;RRID:SCR\_007345.
30. Liu F, Liu C, Zhao L, Zhang X, Wu X, Xu X, et al. An open access database for evaluating the algorithms of electrocardiogram rhythm and morphology abnormality detection. *J Med Imag Health Inform*. 2018;8(7):1368–73. doi:10.1166/jmih.2018.2442.
31. Wagner P, Strodthoff N, Bousseljot RD, Kreiseler D, Lunze FI, Samek W, et al. PTB-XL, a large publicly available electrocardiography dataset. *Scientific Data*. 2020;7(1):1–15. doi:10.1038/s41597-020-0495-6.
32. Zheng J, Guo H, Chu H. A large scale 12-lead electrocardiogram database for arrhythmia study (version 1.0.0). *PhysioNet*. 2022;RRID:SCR\_007345. doi:10.1038/s41597-020-0386-x.
33. Grill JB, Strub F, Altché F, Tallec C, Richemond P, Buchatskaya E, et al. koray kavukcuoglu, Remi Munos, and Michal Valko. Bootstrap your own latent—a new approach to self-supervised learning. *Adv Neural Inform Process Syst*. 2020;33:21271–84.
34. Zbontar J, Jing L, Misra I, LeCun Y, Deny S. Barlow twins: self-supervised learning via redundancy reduction. In: International Conference on Machine Learning. London, UK: PMLR; 2021. p. 12310–20.
35. Chen X, Xie S, He K. An empirical study of training self-supervised vision transformers. In: Proceedings of the IEEE/CVF International Conference on Computer Vision. Piscataway, NJ, USA: IEEE; 2021. p. 9640–9.